Hindawi
Advances in Condensed Matter Physics
Volume 2023, Article ID 9580055, 10 pages
https://doi.org/10.1155/2023/9580055

Research Article

Electronic-, Optical-, and Temperature-Dependent Carrier Mobility Simulations of Perovskite-Type Liganded PbS Quantum Dot Array

Kenta Kumakura,[1] Chih-Chieh Chen ,[2] and Tomah Sogabe [1,2,3]

[1]Engineering Department, The University of Electro-Communications, Tokyo 182-8585, Japan
[2]Grid Inc., Tokyo 107-0061, Japan
[3]i-PERC, The University of Electro-Communications, Tokyo 182-8585, Japan

Correspondence should be addressed to Tomah Sogabe; sogabe@uec.ac.jp

Received 29 March 2023; Revised 17 July 2023; Accepted 2 August 2023; Published 17 August 2023

Academic Editor: Sergio Ulloa

Recent experimental results suggest that higher mobility of perovskite-type ligand passivated PbS quantum dots (QDs) could be useful for efficient solar cell applications. However, theoretical understanding of the mechanism through first principal modeling is still lacking. In this study, electronic-, optical-, and temperature-dependent carrier mobility for perovskite ligand passivated PbS QD array is calculated by using the first-principles density functional theory (DFT) combined with the nonequilibrium Green's function (NEGF) technique and a molecular dynamics (MD)-Landauer approach. It is found that formamidinium (FA)-liganded QDs have higher mobility and enhanced optical absorption comparing to that of Cl-liganded QDs. The difference could be understood through the intermediate band featured electronic structure.

1. Introduction

Harvesting energy directly from solar photons has been a central topic in the quest for sustainable energy. Perovskite-type liganded quantum dots (QDs) solar cells have been investigated extensively for next-generation photovoltaic applications [1, 2]. QD-based intermediate band optoelectronic materials have important effects on the photovoltaic device efficiency [3–5]. On one hand, introducing the intermediate band through QD nanostructure could introduce extra channel for photon absorption to improve the energy conversion efficiency through the increase of the short-circuit current [4]. On the other hand, the change of mobility gives competing effect at short-circuit condition and open-circuit condition due to charge recombination [6]. Understanding the interplay between optical and transport properties regarding the interface effect and ligand effect provides insight in the trade-off for the design of low-dimensional photoelectronic devices [7–9]. Recent studies have experimentally reported higher mobility of perovskite-type liganded PbS QDs [7]. However, theoretical principle regarding the enhancement of mobility has not been revealed, making it difficult to further systemically design and tailor the device performance.

Carrier transport property of formamidinium (FA) lead halide perovskite crystal was previously studied for solar cell applications, but the QD array was not considered [10]. Organic ligand for metal halide perovskite solar cells was discussed and potential application to QDs was conjectured [11]. The application of perovskites nanocrystal instead of QDs was also proposed [12]. Optical properties of colloidal PbS QDs were calculated and experimentally measured, but carrier transport property of QD array was not included in these reports [13, 14]. Carrier transport properties of QD arrays were theoretically studied under various idealized situations, which are different from the focus of this study. For example, Green's functions were calculated for noninteracting systems or small interacting systems, but realistic phonon simulations were not included in these studies [15, 16]. The electronic, optical, and transport properties of PbS QD array are calculated using semiclassical Boltzmann equation for carrier transport [17]. The $k \cdot p$ and drift-diffusion methods were conducted for transportation through QD array junctions [18]. The midgap state effect on the optoelectronic properties of different types of ligand passivated PbS colloidal QDs is studied experimentally with density functional theory (DFT) simulations [19]. Our work is based on molecular dynamics (MD)-Landauer approach, which is different from all the methods mentioned above and will be given in full description in the subsequent section [20–22].

In this work, numerical simulation of the electronic properties, optical absorption, as well as temperature-dependent mobility of organic perovskite-type liganded PbS QDs is performed while taking the halogen (here Cl) liganded PbS QDs as a reference. It is observed in simulations that the carrier mobility of FA-liganded QDs is higher than that of Cl-liganded QDs for a wide range of temperature. Further, calculations of electronic structure and optical absorption suggest that the existence or absence of intermediate band plays a role in the change of transport property. Intuitively, the intermediate band provides extra channel of relaxation through scattering, and, hence, could hinder the carrier transport. Our simulation results provide evidence for this intuition and a guide for future development of perovskite-liganded QD solar cells.

This paper is organized as follows. The details of calculation methods and parameters for simulations are listed in Section 2. The main results and discussion are presented in Section 3. The conclusion is given in Section 5.

2. Simulation Methods

2.1. Electronic Structure and Optical Simulation. The geometry of the liganded QDs is optimized through QuantumATK software [23]. In QuantumATK software, global structural optimization is implemented through a genetic algorithm. It works by generating an initial set of random configurations and then evolving them using genetic operators [24]. The electronic structure and optical properties were calculated by using density functional theory-linear combination of atomic orbitals (DFT-LCAO) method embedded in QuantumATK software [25]. The simulation details and initial parameters setting are listed in Table S1.

2.2. MD-Landauer Method for Simulating Mobility. Combining molecular dynamics simulation with nonequilibrium Green's function (NEGF) for quantum transport gives the so-called MD-Landauer method [20–22]. QuantumATK software is used for the calculations [23]. Electron–phonon coupling (EPC) plays a key role in the performance of most electronic devices. However, rigorous simulation of EPC is both challenging for the approaches either based on the first principle or Boltzmann transport equation and for device based on both bulk materials and nano- or atomic-scale materials [26–28]. One of the most concerning drawbacks of these conventional approaches, such as the EPC in the Boltzmann equation and the perturbative NEGF methods, is the harmonic approximation of phonons, since introducing anharmonic effects would dramatically increases the computational cost. However, the anharmonic contributions to the phonons are strong at room temperatures and above for many materials, which could not be deal properly with these conventional approaches [22]. In this framework, the electron–phonon interaction is taken into account through the MD calculation, while the carrier transport properties are calculated by DFT-NEGF method and Landauer formula. Figure 1 shows the sketched principle for the proposed methods. For device structure with fixed left and right electrodes, the central transportation region was subjected to MD simulation under different temperature and corresponding NEGF to derive the conductance $G(\ell, T)$ based on transmittance $\mathcal{T}_{\ell}(E, T)$. Figures 1(a) and 1(b) show the device structure with short and long length of the MD region. Figure 1(c) illustrates the simulation flowchart of MD-Landauer method. Started with a specified length of the MD region, the equilibrium lattice structure is obtained for the central region at the specified temperature T. DFT-NEGF method is then applied to calculate the length-dependent transmittance $\mathcal{T}_{\ell}(E, T)$, averaged over the MD samples based on the following Landauer formula to simulate the conductance $G(\ell, T)$:

$$G(\ell, T) = \frac{2e^2}{h} \int \langle T_{\ell}(E, T) \rangle \left(-\frac{\partial f\left(E, E_f, T\right)}{\partial E} \right) dE, \tag{1}$$

where e is the elementary charge, h is Planck's constant, and E_f is the Fermi-level energy. The Landauer formula is used to obtain the conductance and resistance based on the following equations:

$$R(\ell, T) = \frac{1}{G(\ell, T)}. \tag{2}$$

As shown in Figure 1(c), this process was repeated for different length of MD region. Here, we have performed four different lengths indexed with l_0, l_3, l_4, l_5 and the numbers 0, 3, 4, and 5 represent the number of liganded QDs located between the two electrodes. With the resistance under different length of MD region, the 1 D resistivity $\rho_{1D}(T)$ is then to be extracted from linear regression over samples of different lengths ℓ using the conventional least square regression algorithm.

$$R(\ell, T) = R_c + \rho_{1D}(T)\ell + \varepsilon, \ \ \varepsilon \in N(0, 1), \tag{3}$$

$$\rho_{1D}(T) = \frac{N \sum_{i=1}^{N} \ell^i \cdot R(\ell^i, T) - \sum_{i=1}^{N} \ell^i - \sum_{i=1}^{N} R(\ell^i, T)}{N \sum_{i=1}^{N} (\ell^i)^2 - \left(\sum_{i=1}^{N} \ell^i \right)^2}, \tag{4}$$

where ε is defined as random number from normal distribution $Normal(0, 1)$ and N is the number of sample data, here $N = 3$. The procedure is repeatedly performed for MD central region with different lengths, so that the resistivity $\rho_{1D}(T)$ can be obtained by linear regression based on the Formula (4). Using the results of $\rho_{1D}(T)$, the mobility can readily be calculated as follows:

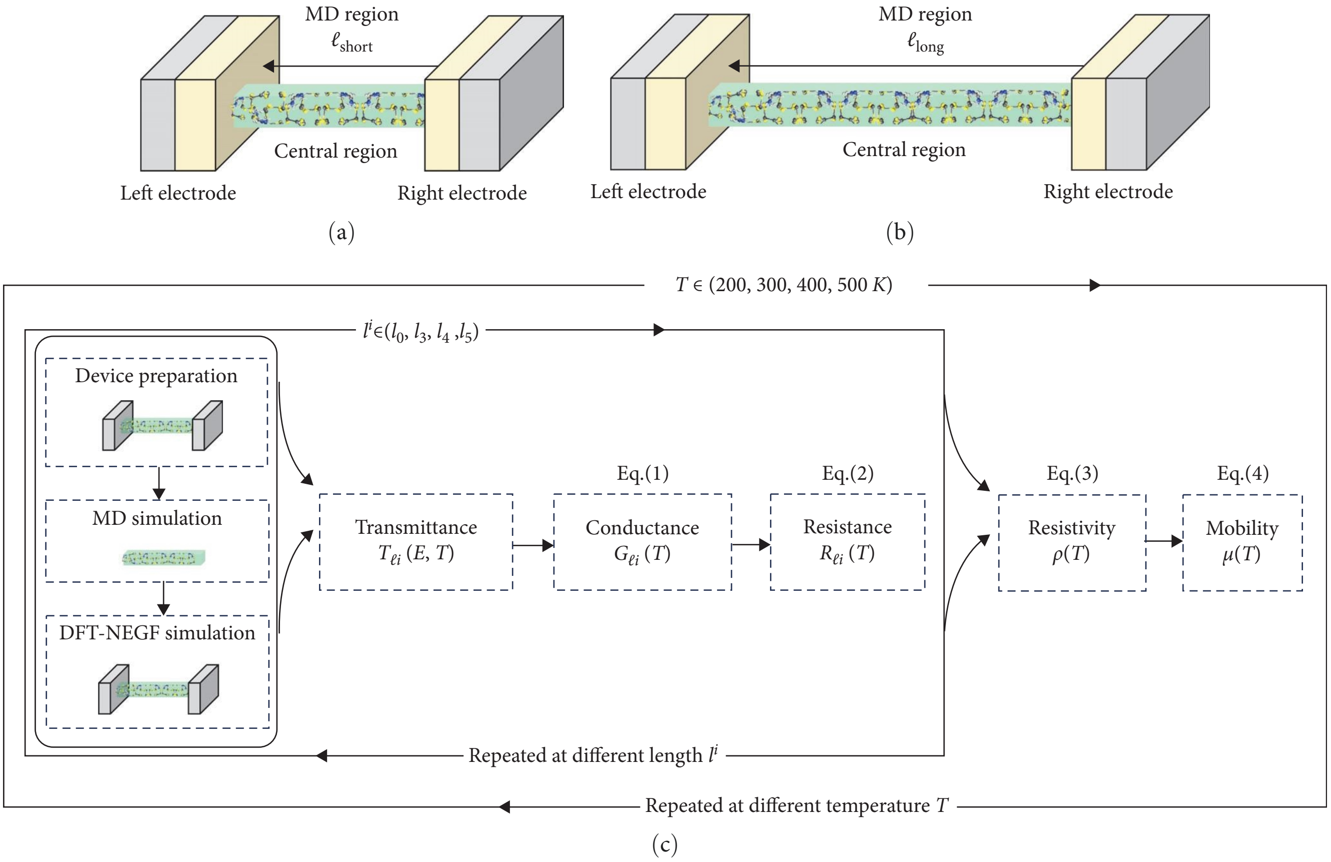

Figure 1: Sketch of device structure used in MD-Landauer method. (a) QD array transportation device structure with short MD region. (b) QD array transportation device structure with long MD region. (c) Flowchart of the temperature-dependent mobility simulation using MD-Landauer method.

$$\mu(T) = \frac{1}{en\,\rho_{\text{bulk}}(T)}, \tag{5}$$

where n is the carrier density. $\rho_{\text{bulk}} = A\rho_{1D}$ is the bulk resistivity and is calculated with a predetermined device cross-section area A. The mobility $\mu(T)$ under specified temperature T is obtained and the whole procedure is repeatedly conducted for other temperatures, as shown in Figure 1(c). The parameters used in our MD-Landauer simulations are listed in Table S2 and will be given in more detailed explanation in next section.

3. Results and Discussion

3.1. The Structures of Simulated Systems. The electronic and optical properties of PbS QD arrays without ligand, with FA ligand, and with Cl ligand are studied and compared. Ten ligands are added to one QD for both FA and Cl cases. The structures of the QDs are depicted in Figure 2(a). The geometries of the QDs for both FA ligand and Cl ligand are optimized with DFT-LCAO method from a randomized initial structure, where the detail of the optimization algorithm is presented in the Method section. The QDs are arranged on a square lattice of unit cell (1×1) with periodic boundary. The distances between QDs are set as 1.7 nm, which has been verified as the maximum distance that shows a coupling effect between QDs in the band structure (see Figure S1 for the results of the QD distance larger than 1.7 nm in Appendix for more details). The superlattice for these two ligands are depicted in Figure 2(b).

3.2. Electronic and Optical Properties of QD with Ligands. Band structure, density of states (DOS), and optical absorption coefficient are calculated using the DFT package embedded in QuantumATK software. Figure 3(a)–3(c) shows the band structure of QD arrays with different ligands. For better comparison, we also presented the band structure simulation results for the PbS QDs without ligand, as shown in Figure 3(a). A well-defined Fermi level is found located at the middle of the band gap indicating the intrinsic semiconductor feature of the proposed structures. It is observed, as shown in Figures 3(a) and 3(c), that the intermediate bands located between the energy range of 0.5 and 1.0 eV exist for both pure PbS QD array and and Cl-liganded QD array. However, striking difference was found for the band structure of FA-liganded QD array, as shown in Figure 3(b), where there is no feature indicating the formation of intermediate band and instead band continuum was formed with the lowest band edge at the energy around ~0.6 eV. It can also be verified from the DFT band structure simulation that FA-liganded PbS QD array possesses an energy bandgap of 1.28 eV, which is about 0.37 eV narrower

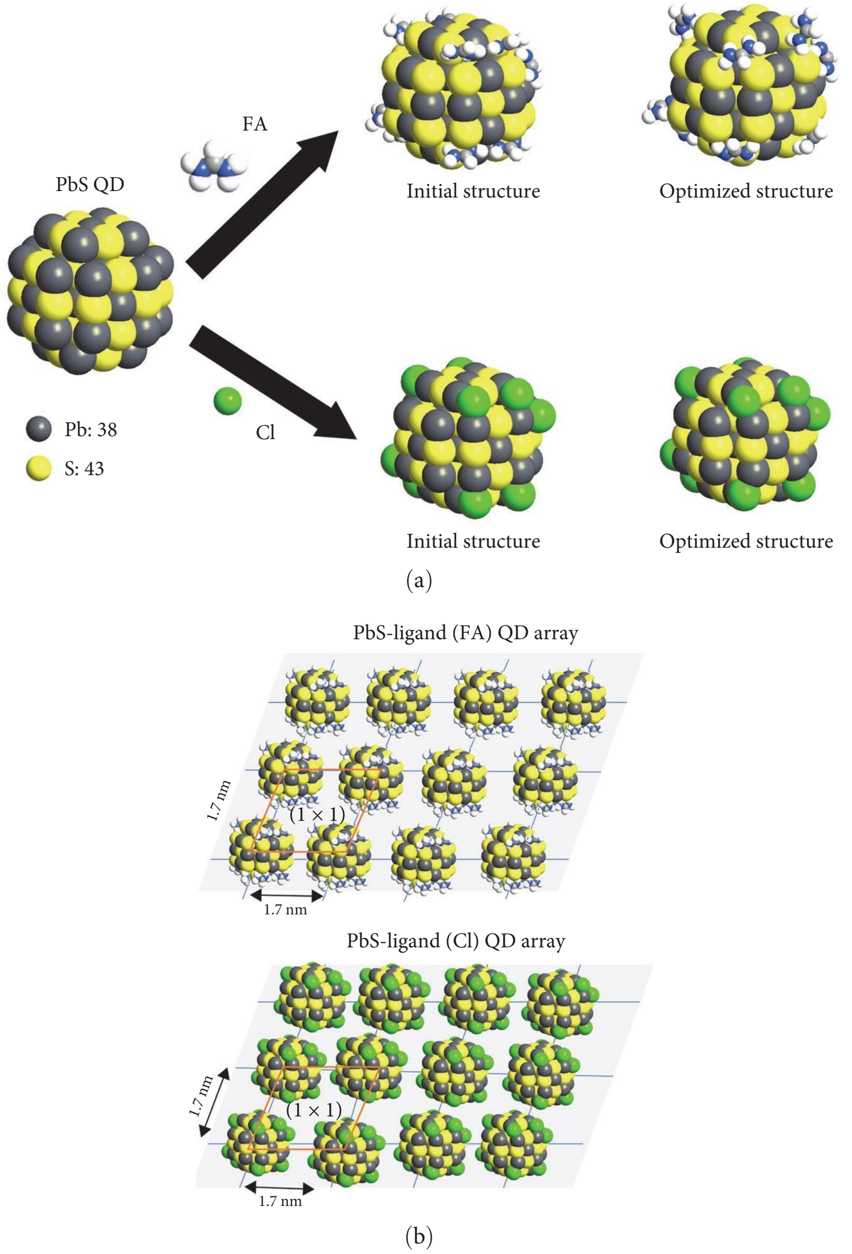

Figure 2: The QDs with different ligands in this study. Each solid sphere denotes one atom. (a) The geometry of the liganded QDs is numerically optimized to minimize the self-consistent energy. (b) The QD superlattices for both FA ligand and Cl ligand are constructed with unit cell (1×1) for simulations of various properties.

than energy bandgap of 1.65 eV for the PbS QD array without ligand. Different from the FA-liganded, the Cl-liganded PbS QD array, which has bandgap energy of 1.48 eV and the intermediate band in the range between 0.5 and 1.0 eV, more closely resembles the electronic band structure to the ones of PbS QD without ligand.

To further understand these phenomena, we investigated the DOS and optical absorption profile. Figure 4(a)–4(f) shows the calculated DOS, optical absorption, and orbital-projected PDOS for the FA-liganded and Cl-liganded QDs. It has been reported that PbS QD excitonic peak could smear out due to hybridization of orbitals [29]. In our DOS simulation data, a separated conduction band peak near the Fermi level for Cl-liganded QD is observed (highlighted by red-dashed circle, as shown in Figure 4(d)). This peak does not exist in the FA-liganded QD DOS (Figure 4(a)), and FA-liganded QD has generally higher DOS at conduction band. This difference in the DOS could indeed affect the optical properties of the QD lattice, as confirmed by the optical absorption data (Figures 4(b) and 4(e)). The optical absorption coefficient of Cl-liganded QD also has an isolated peak near 1.5 eV (highlighted by red-dashed circle, as shown in Figure 4(e)), but the peak is not observed in the FA-liganded QD data. The FA-liganded optical coefficient has higher value around 1.75 eV than that of Cl-liganded QD. This difference could be further understood by comparing orbital-projected

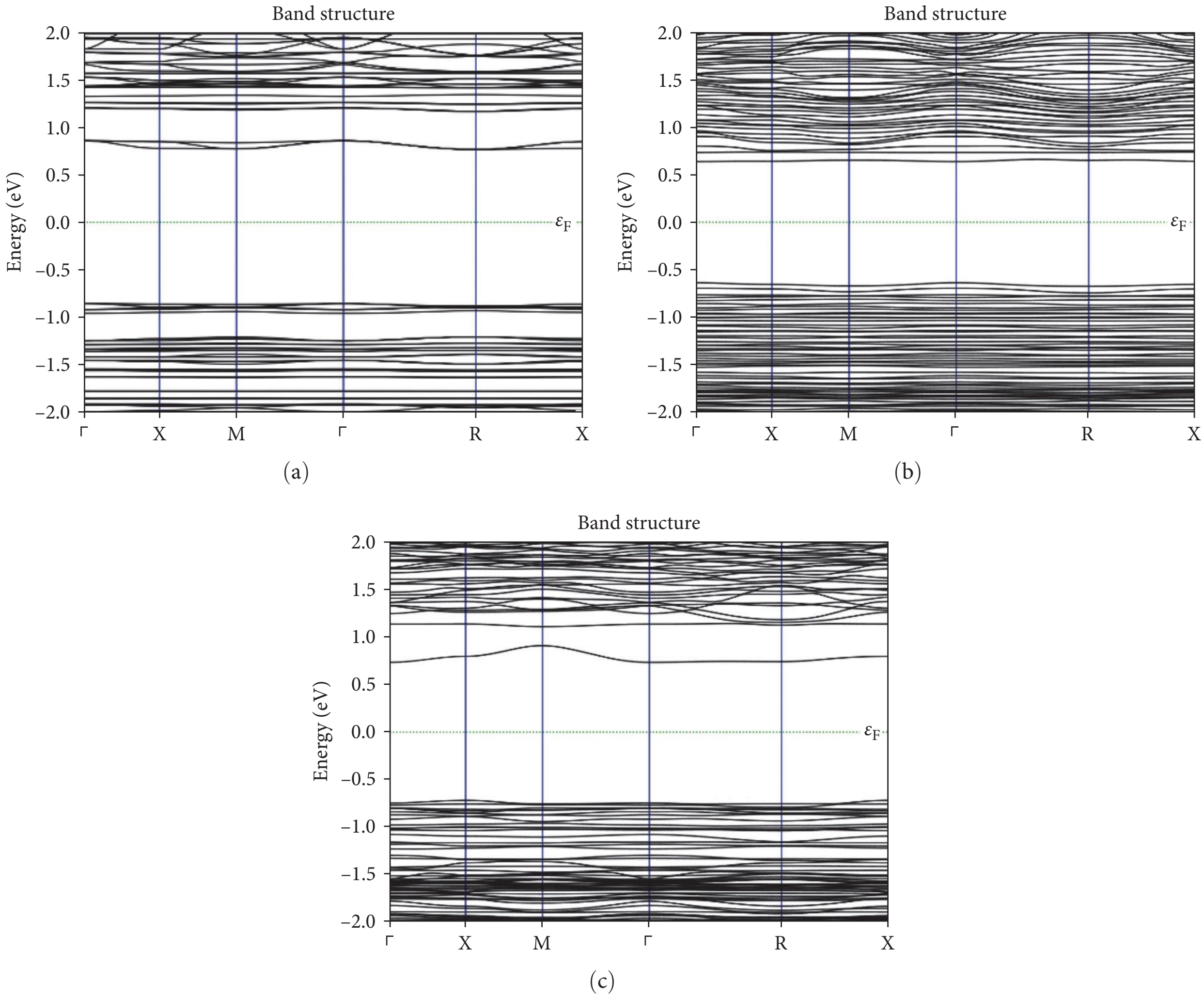

(a)

(b)

(c)

Figure 3: The calculated band structures for QDs. The intermediate bands are colored by pink shadow. (a) Band structure for QD without ligand. The bandgap is 1.647 eV. (b) Band structure for QD with FA ligand. The bandgap is 1.280 eV. (c) Band structure for QD with Cl ligand. The bandgap is 1.477 eV.

DOS (Figures 4(c) and 4(f)). The 2p – orbital DOS of FA-liganded QD has one extra peak over the energy range of 0.6–2.0 eV in conduction band, while this peak does not exist for Cl ligand. The hybridization with 2p – orbital could be the reason of the absence of intermediate band for FA-liganded QD.

3.3. Temperature-Dependent Carrier Mobility for FA-Liganded PbS QD Array. To understand the carrier transport properties of the QD arrays, mobility of QD array junctions is calculated by using the MD-Landauer method for a wide range of temperatures. Figure 5 depicts the structure of the junctions with the element of left and right electrode, as well as the central MD region. The 1D QD array is sandwiched by two $CH(NH_2)_2PbI_3$ perovskite electrodes. Figure 5(a)–5(c) showed single FA-ligand QD, double FA-liganded QDs, and triple FA-liganded QDs. Figure 5(d)–5(f) corresponded to the single Cl-liganded QD, double Cl-liganded QDs, and triple Cl-liganded QDs, respectively. This method is described in Section 2 and Formula (1)–(5). The conductance $G(\ell, T)$ of a junction with MD central region length ℓ and temperature T is obtained. To adopt the Formula (5), the bulk resistivity has to be calculated in advance using the formula $\rho_{\text{bulk}} = A\rho_{1D}$. Here, the area A is fixed to the calculated value of $375.58(^\circ A^2)$ in all the simulations. Due to the space limit, we present all the detailed simulation information for deriving the temperature dependent in the Supplementary Materials. Table S2 summarized all the parameters for MD-Landauer calculation. Table S3 provided the carrier density value of n used in Formula (5) for both FA- and Cl-liganded PbS QD arrays under different temperatures. The carrier density was calculated by QuantumATK software with parameters: contribution = electron and Fermi shift = 0.13 eV. Table S4 presented the size information characterizing the MD region. Three types of MD region containing one QD, two QDs, and three QDs were prepared and labeled as L_3, L_4, L_5, respectively, while the PbS QD without ligand was labeled as L_0. Tables S5 and S6 summarized all the resistance data for

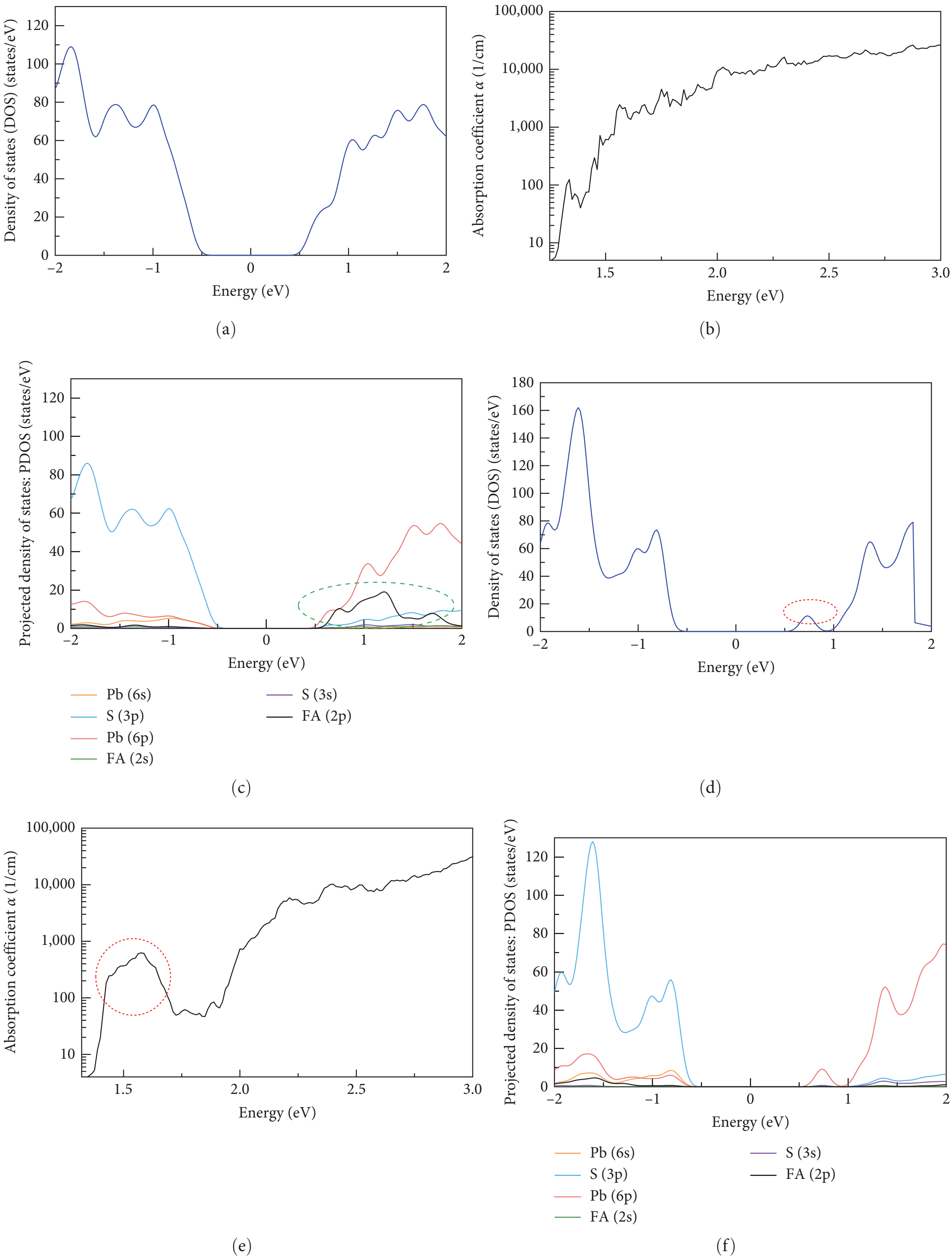

FIGURE 4: The density of states (DOS), optical absorption, and orbital-projected DOS for FA-liganded QD and Cl-liganded QD. (a) The optical absorption of FA-liganded QD. (b) The DOS of FA-liganded QD. (c) The orbital-projected DOS for FA-liganded QD. The hybridization effect of FA p-orbital DOS (black solid line) in the conduction band is highlighted with a green-dashed square. (d) The optical absorption of Cl-liganded QD. The contribution of the intermediate band is highlighted with a red-dashed circle. (e) The DOS of Cl-liganded QD. The contribution of the intermediate band is highlighted with a red-dashed circle. (f) The orbital-projected DOS for Cl-liganded QD. The FA p-orbital DOS (black solid line) does not show the hybridization effect in the conduction band.

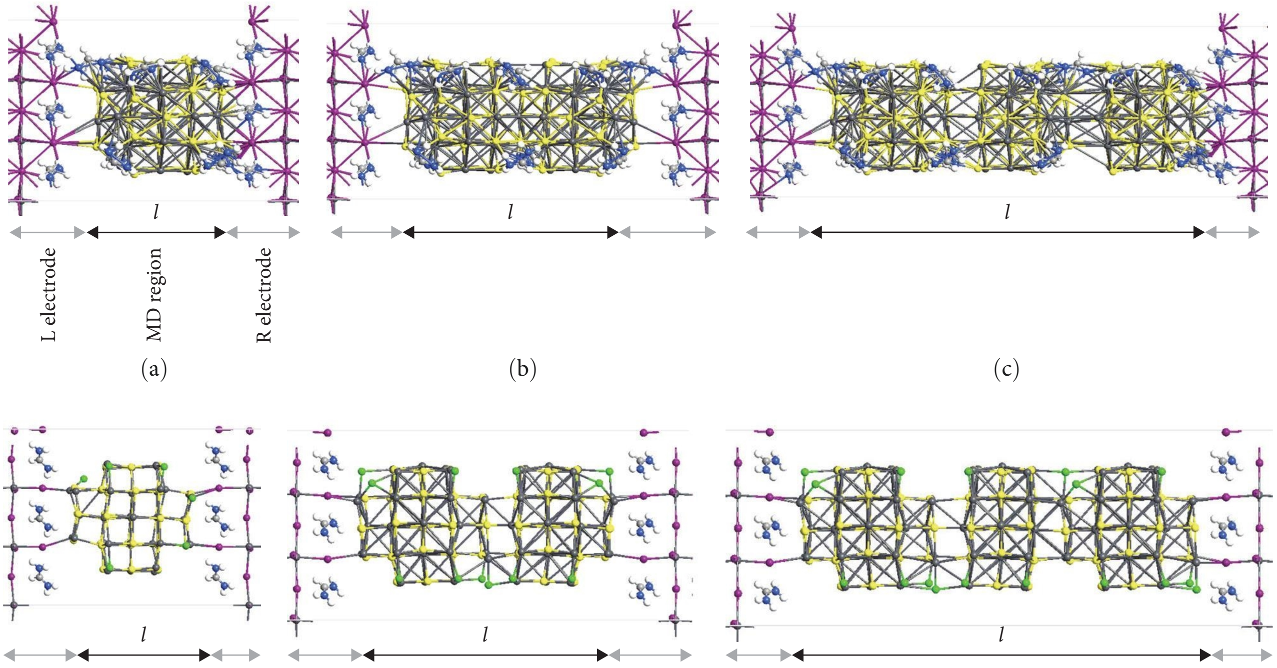

(a) (b) (c) (d) (e) (f)

Figure 5: The QD array junctions with different numbers of QDs and different QD array lengths. The one-dimensional PbS QD arrays are the middle region for MD-Landauer calculations. The electrodes are $CH(NH_2)_2PbI_3$. (a) Single FA-liganded QD. (b) Double FA-liganded QDs. (c) Triple FA-liganded QDs. (d) Single Cl-liganded QDs. (e) Double Cl-liganded QDs. (f) Triple Cl-liganded QDs.

Cl-liganded PbS QD and FA-liganded PbS QD for performing linear regression and derivation of the resistivity. The length- and temperature-dependent transmittance $\mathcal{T}_{\ell}(E, T)$ for bare PbS QD, FA-liganded sample, as well as Cl-liganded sample was summarized in Figure S2. Notice that we have only presented the results simulated at 300 K as an example in Figure S2. In addition, attention must be paid when interpreting the transmittance data, as shown in Figure S2, because the transmittance data alone is not proportional to the carrier mobility and the energy integrated transmittance, namely, the conductance $G(\ell, T)$ is used to prepare the resistance data for deriving the resistivity $\rho_{1D}(T)$, which is in fact inverse proportional to the carrier mobility $\mu(T)$. Figures 6(a) and 6(b) show the simulation and regression data for FA-liganded QDs and Cl-liganded QDs, respectively, by taking the temperature condition of 300 K as an example. Figure 6(c) showed the log-linear plot of the mobility calculated by the Formula (5) using the parameters listed in Table S2–S6. It can be clearly seen from Figure 6(c) that FA-liganded QD (red solid line with circle marker) has higher mobility than that of Cl-liganded QD (blue solid line with square marker) near the room temperature. For FA-liganded QDs at 300 K, the resistivity of $\rho_{\text{bulk}} = 102,000\ (\Omega \cdot \text{m})$ was derived by linearly fitting the data, as shown in Figure 6(a), using the Formula (4) and the mobility was simulated as $\mu = 0.001394(\text{cm}^2 \cdot \text{V}^{-1} \cdot \text{s}^{-1})$ by using Formula (5) where the carrier density $n = 4.39 \times 10^{14}(\text{cm}^{-3})$ was used. For Cl-liganded QDs at 300 K, the resistivity is $\rho_{\text{bulk}} = 748,000\ (\Omega \cdot \text{m})$ by fitting the data, as shown in Figure 6(b), using the Formula (4) and the mobility is $\mu = 0.0001481(\text{cm}^2 \cdot \text{V}^{-1} \cdot \text{s}^{-1})$ by using the carrier density $n = 5.635 \times 10^{14}(\text{cm}^{-3})$. The numerical data of the other temperatures for both FA- and Cl-liganded PbS QDs could be found in Table S3, Table S4, Table S5, and Table S6 in Supplementary Materials.

4. Discussion

In the simulation data, both the mobilities of FA-liganded QD arrays and Cl-liganded QD arrays decrease with the increase of the temperature. Similar temperature-dependent behavior has been reported in the mobilities simulation of the silicon bulk material and silicon nanowire using the same approach [22]. Meanwhile, it is found that the FA-liganded PbS QD arrays have generally higher mobility than that of Cl-liganded QD arrays for a wide range of temperatures. The enhanced mobility appeared in FA-liganded PbS QD could be attributed to the following factors:

(1) The difference in transport property could be explained by the corresponding band structure calculation, as shown in Figures 2(a) and 2(b), which indicates the disappearance of intermediate band in FA-liganded QD arrays. This fact also affects the optical absorption data, where FA-liganded QDs have a bulk-like absorption profile with no isolated peak and a higher optical absorption value than that of Cl-liganded QDs. Our DOS data suggests that the disappearance of discrete feature in FA-liganded sample could be related to the hybridization of 2p orbitals. We claim that the FA-liganded QD arrays

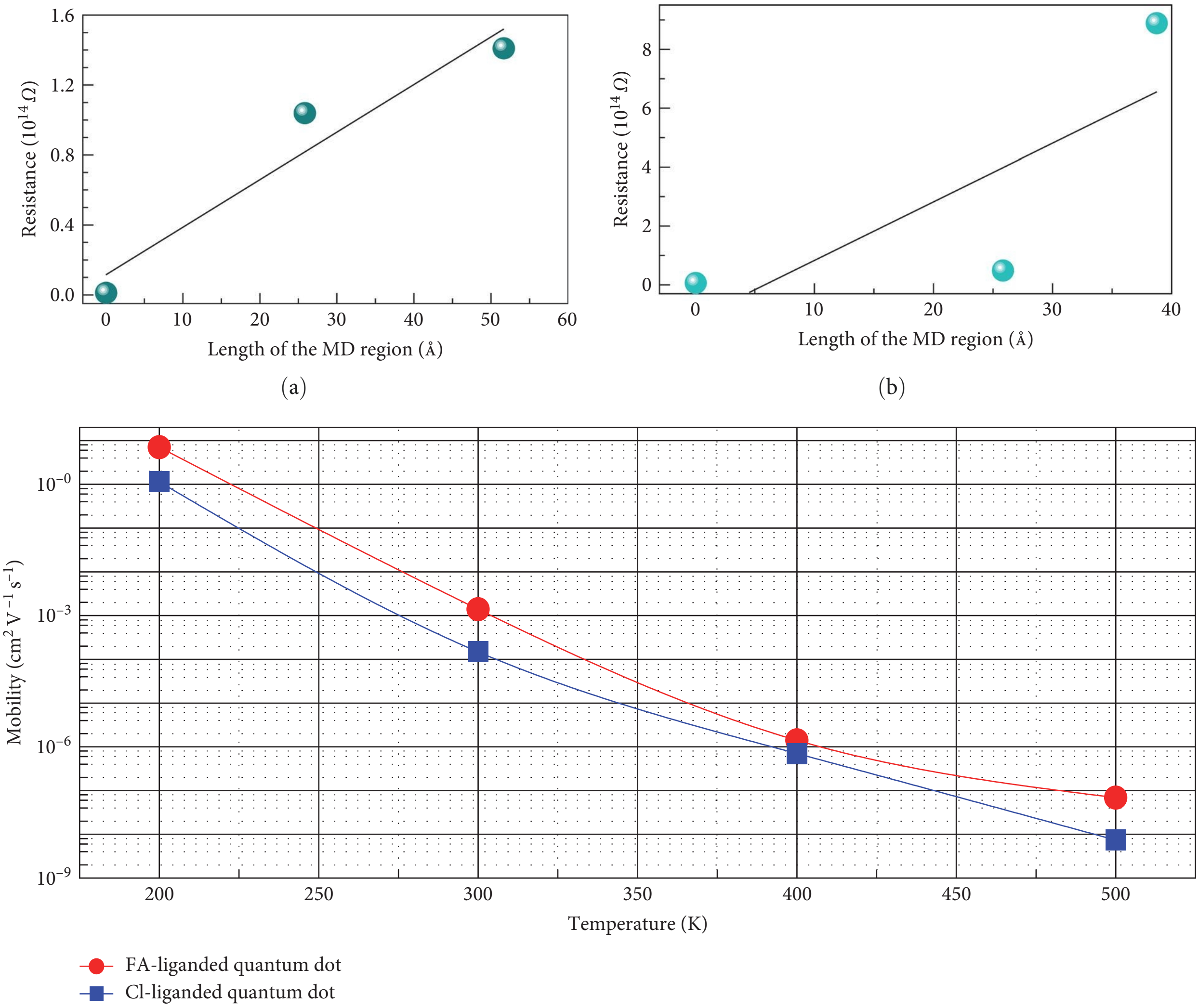

(a)

(b)

(c)

Figure 6: (a) Resistance with respect to the length of the MD region for FA-liganded QD array junction. The y-scale is in $10^{14}\,\Omega$. Linear regression (red solid line) is performed to extract the resistivity $\rho_{\text{bulk}} = 102,000\,(\Omega\cdot\text{m})$. The temperature is 300 K. (b) Resistance with respect to the length of the MD region for Cl-liganded QD array junction. The y-scale is in $10^{14}\,\Omega$. Linear regression (red solid line) is performed to extract the resistivity $\rho_{\text{bulk}} = 748,000\,(\Omega\cdot\text{m})$. The temperature is 300 K. (c) Log-linear plot of the mobility with respect to temperature. FA-liganded QD (red solid line with circle marker) has higher mobility than that of Cl-liganded QD (blue solid line with square marker) near the room temperature.

showed much stronger continuum band featured bulk-like electronic property than the Cl-liganded ones, where the quantum size effect-induced discrete energy features are still dominating. As demonstrated in literatures [22, 30], it has been confirmed both experimentally and theoretically that bulk silicon showed about one order higher mobility than its counterpart of silicon nanowire. In our work, the absolute difference between the mobility of FA- and Cl-liganded sample is quite small, which indicates that although the bulk feature in FA-liganded PbS QD prevails, the effect is still weak.

(2) Based on the mobility calculation Formula (5), it is found that the carrier density plays equal role as the resistivity. By closely examining the carrier density simulated for both FA- and Cl-liganded PbS QD array, we found that the carrier density in FA-liganded sample is much less than the Cl-liganded sample. The bandgap value of FA-liganded sample is the smallest when compared to the values of bare PbS QD array and Cl-liganded QD array, as shown in Figures 2(a) and 2(b). One would expect larger carrier density in FA-liganded sample due to the narrower bandgap. However, the simulated carrier density based on rigorous extraction from the DFT simulation showed opposite tendency. We attribute this effect to the multiple energy bands appeared in both the bare PbS QD array sample and Cl-liganded sample. Additional intermediate band provides additional channel for carrier generations, which is exactly the

appealing feature for intermediate band solar cell. However, as suggested in the mobility simulation, the enhanced carrier density will inevitably cause the reduction of mobility, which is exactly the primal obstacle, which has been shown both experimentally and theoretically to hinder the realization of the high-efficiency intermediate band solar cell [31–33]. In the optimization of power generation of photovoltaic devices, both carrier transport and optical properties should be considered. The calculation in this study provides a fundamental guide for better design of solar cell devices.

5. Conclusions

In this study, we theoretically analyzed the electronic, optical properties and temperature-dependent mobility of QDs with FA ligand by taking the Cl ligand as a reference. FA-liganded PbS QDs showed larger optical absorption coefficients due to the elimination of intermediate levels or band. Mobility simulation results verified that the mobility in FA ligand is larger than the Cl ligand. Our work revealed a novel type of mobility enhancement originated from orbit overlapping, which could provide important information for further device improvement.

Data Availability

All the simulation codes for reproducing the simulation results are available from the corresponding author on reasonable request.

Conflicts of Interest

The authors declare that they have no conflicts of interest.

Acknowledgments

The authors gratefully acknowledge the funding from New Energy and Industrial Technology Development Organization (NEDO) (Grant Number JPNP20015) and the Ministry of Economy, Trade and Industry (METI), Japan.

Supplementary Materials

Table S1: lists the parameters for DFT-LCAO calculation. Table S2: lists the parameters for MD-Landauer calculation. Table S3: records the carrier density. Table S4: shows the lengths of MD regions. Tables S5 and S6: shows the regression data for Cl ligand and FA ligand, respectively. Figure S1: contains the band structure comparison for different inter-QD distances. Figure S2: shows carrier transmittance for simulating mobility. (*Supplementary Materials*)

References

[1] S. Ding, M. Hao, T. Lin, Y. Bai, and L. Wang, “Ligand engineering of perovskite quantum dots for efficient and stable solar cells,” *Journal of Energy Chemistry*, vol. 69, pp. 626–648, 2022.

[2] M. Hao, Y. Bai, S. Zeiske et al., “Ligand-assisted cation-exchange engineering for high-efficiency colloidal $Cs_{1-x}FA_xPbI_3$ quantum dot solar cells with reduced phase segregation,” *Nature Energy*, vol. 5, pp. 79–88, 2020.

[3] A. Luque and A. Martí, “Increasing the efficiency of ideal solar cells by photon induced transitions at intermediate levels,” *Physical Review Letters*, vol. 78, no. 26, pp. 5014–5017, 1997.

[4] Y. Okada, T. Sogabe, and Y. Shoji, “Intermediate band solar cells,” in *Energy and Environment Series*, A. J. Nozik, G. Conibeer, and M. C. Beard, Eds., pp. 425–454, Royal Society of Chemistry, Cambridge, 2014.

[5] I. Ramiro, A. Marti, E. Antolin, and A. Luque, “Review of experimental results related to the operation of intermediate band solar cells,” *IEEE Journal of Photovoltaics*, vol. 4, no. 2, pp. 736–748, 2014.

[6] J.-T. Shieh, C.-H. Liu, H.-F. Meng, S.-R. Tseng, Y.-C. Chao, and S.-F. Horng, “The effect of carrier mobility in organic solar cells,” *Journal of Applied Physics*, vol. 107, no. 8, Article ID 084503, 2010.

[7] B. Sun, A. Johnston, C. Xu et al., “Monolayer perovskite bridges enable strong quantum dot coupling for efficient solar cells,” *Joule*, vol. 4, no. 7, pp. 1542–1556, 2020.

[8] C.-H. Yeh, H.-C. Chen, H.-C. Lin et al., “Ultrafast monolayer In/Gr-WS_2-Gr hybrid photodetectors with high gain,” *ACS Nano*, vol. 13, no. 3, pp. 3269–3279, 2019.

[9] R. Hou, Y. Xia, and S. Yang, “A linear relationship between the charge transfer amount and level alignment in molecule/two-dimensional adsorption systems,” *ACS Omega*, vol. 5, no. 41, pp. 26748–26754, 2020.

[10] A. A. Zhumekenov, M. I. Saidaminov, M. A. Haque et al., “Formamidinium lead halide perovskite crystals with unprecedented long carrier dynamics and diffusion length,” *ACS Energy Letters*, vol. 1, no. 1, pp. 32–37, 2016.

[11] H. Zhang, M. K. Nazeeruddin, and W. C. H. Choy, “Perovskite photovoltaics: the significant role of ligands in film formation, passivation, and stability,” *Advanced Materials*, vol. 31, no. 8, Article ID 1805702, 2019.

[12] F. Haydous, J. M. Gardner, and U. B. Cappel, “The impact of ligands on the synthesis and application of metal halide perovskite nanocrystals,” *Journal of Materials Chemistry A*, vol. 9, no. 41, pp. 23419–23443, 2021.

[13] I. Moreels, K. Lambert, D. Smeets et al., “Size-dependent optical properties of colloidal PbS quantum dots,” *ACS Nano*, vol. 3, no. 10, pp. 3023–3030, 2009.

[14] L. Cademartiri, E. Montanari, G. Calestani, A. Migliori, A. Guagliardi, and G. A. Ozin, “Size-dependent extinction coefficients of PbS quantum dots,” *Journal of the American Chemical Society*, vol. 128, no. 31, pp. 10337–10346, 2006.

[15] M.-H. Cha and J. Hwang, “Quantum transport in a chain of quantum dots with inhomogeneous size distribution and manifestation of 1D anderson localization,” *Scientific Reports*, vol. 10, Article ID 16701, 2020.

[16] B. R. Bułka and T. Kostyrko, “Electronic correlations in coherent transport through a two quantum dot system,” *Physical Review B*, vol. 70, no. 20, Article ID 205333, 2004.

[17] Y. Liu, N. Peard, and J. C. Grossman, “Bandlike transport in PbS quantum dot superlattices with quantum confinement,” *The Journal of Physical Chemistry Letters*, vol. 10, no. 13, pp. 3756–3762, 2019.

[18] T. Sogabe, T. Kaizu, Y. Okada, and S. Tomić, “Theoretical analysis of GaAs/AlGaAs quantum dots in quantum wire array for intermediate band solar cell,” *Journal of Renewable and Sustainable Energy*, vol. 6, no. 1, Article ID 011206, 2014.

[19] A. H. Ip, S. M. Thon, S. Hoogland et al., "Hybrid passivated colloidal quantum dot solids," *Nature Nanotechnology*, vol. 7, pp. 577–582, 2012.

[20] R. Landauer, "Spatial variation of currents and fields due to localized scatterers in metallic conduction," *IBM Journal of Research and Development*, vol. 1, no. 3, pp. 223–231, 1957.

[21] L. P. Kadanoff and G. Baym, *Quantum Statistical Mechanics: Green's Function Methods in Equilibrium and Nonequilibrium Problems*, CRC Press, 1st edition, 2018.

[22] T. Markussen, M. Palsgaard, D. Stradi, T. Gunst, M. Brandbyge, and K. Stokbro, "Electron-phonon scattering from green's function transport combined with molecular dynamics: applications to mobility predictions," *Physical Review B*, vol. 95, no. 24, Article ID 245210, 2017.

[23] S. Smidstrup, T. Markussen, P. Vancraeyveld et al., "QuantumATK: an integrated platform of electronic and atomic-scale modelling tools," *Journal of Physics: Condensed Matter*, vol. 32, no. 1, Article ID 015901, 2020.

[24] C. W. Glass, A. R. Oganov, and N. Hansen, "USPEX—evolutionary crystal structure prediction," *Computer Physics Communications*, vol. 175, no. 11-12, pp. 713–720, 2006.

[25] P. Hohenberg and W. Kohn, "Inhomogeneous electron gas," *Physical Review*, vol. 136, no. 3B, pp. B864–B871, 1964.

[26] R. Rhyner and M. Luisier, "Atomistic modeling of coupled electron–phonon transport in nanowire transistors," *Physical Review B*, vol. 89, no. 23, Article ID 235311, 2014.

[27] C.-H. Park, N. Bonini, T. Sohier et al., "Electron–phonon interactions and the intrinsic electrical resistivity of graphene," *Nano Letters*, vol. 14, no. 3, pp. 1113–1119, 2014.

[28] K. Kaasbjerg, K. S. Thygesen, and K. W. Jacobsen, "Unraveling the acoustic electron–phonon interaction in graphene," *Physical Review B*, vol. 85, no. 16, Article ID 165440, 2012.

[29] A. Pimachev and Y. Dahnovsky, "Optical and magnetic properties of PbS nanocrystals doped by manganese impurities," *The Journal of Physical Chemistry C*, vol. 119, no. 29, pp. 16941–16946, 2015.

[30] K. Mao, T. Saraya, and T. Hiramoto, "Effects of side surface roughness on carrier mobility in tri-gate single silicon nanowire metal–oxide–semiconductor field-effect transistors," *Japanese Journal of Applied Physics*, vol. 52, no. 4S, Article ID 04CC11, 2013.

[31] T. Sogabe, C.-Y. Hung, R. Tamaki et al., "Experimental demonstration of energy-transfer ratchet intermediate-band solar cell," *Communications Physics*, vol. 4, Article ID 38, 2021.

[32] T. Sogabe, Y. Shoji, M. Ohba et al., "Intermediate-band dynamics of quantum dots solar cell in concentrator photovoltaic modules," *Scientific Reports*, vol. 4, Article ID 4792, 2014.

[33] Y. Okada, N. J. Ekins-Daukes, T. Kita et al., "Intermediate band solar cells: recent progress and future directions," *Applied Physics Reviews*, vol. 2, no. 2, Article ID 021302, 2015.